



HAL
open science

On the Modeling of Thermal Radiation at the Top Surface of a Vacuum Arc Remelting Ingot

P.-O. Delzant, B. Baqué, P Chapelle, A. Jardy

► To cite this version:

P.-O. Delzant, B. Baqué, P Chapelle, A. Jardy. On the Modeling of Thermal Radiation at the Top Surface of a Vacuum Arc Remelting Ingot. *Metallurgical and Materials Transactions B*, 2018, 49 (3), pp.958-968. <10.1007/s11663-018-1194-y>. <hal-02106550>

HAL Id: hal-02106550

<https://hal.science/hal-02106550v1>

Submitted on 13 Jan 2022

HAL is a multi-disciplinary open access archive for the deposit and dissemination of scientific research documents, whether they are published or not. The documents may come from teaching and research institutions in France or abroad, or from public or private research centers.

L'archive ouverte pluridisciplinaire **HAL**, est destinée au dépôt et à la diffusion de documents scientifiques de niveau recherche, publiés ou non, émanant des établissements d'enseignement et de recherche français ou étrangers, des laboratoires publics ou privés.



HAL Authorization

1 **On the modelling of thermal radiation at the top surface of a vacuum arc**
2 **remelting ingot**

3
4 P.-O. Delzant^{1,2}, B. Baqué¹, P. Chapelle¹, A. Jardy¹

5
6 ¹Institut Jean Lamour - UMR 7198 CNRS/Université de Lorraine,
7 Laboratory of Excellence DAMAS, Campus ARTEM, 2 allée André Guinier,
8 54000 Nancy Cedex, France

9 ²TIMET Savoie, Avenue Paul Girod, 73400 Ugine, France
10

11 Keywords: Vacuum Arc Remelting, Thermal radiation, Radiosity method

12 Corresponding author: P. Chapelle pierre.chapelle@univ-lorraine.fr

13 **Abstract**
14

15 Two models have been implemented for calculating the thermal radiation emitted at the ingot
16 top in the VAR process, namely a crude model that considers only radiative heat transfer
17 between the free surface and electrode tip and a more detailed model that describes all
18 radiative exchanges between the ingot, electrode and crucible wall using a radiosity method.
19 From the results of the second model, it is found that the radiative heat flux at the ingot top
20 may depend heavily on the arc gap length and the electrode radius, but remains almost
21 unaffected by variations of the electrode height. Both radiation models have been integrated
22 into a CFD numerical code that simulates the growth and solidification of a VAR ingot. The
23 simulation of a Ti-6-4 alloy melt shows that use of the detailed radiation model leads to some
24 significant modification of the simulation results as compared to the simple model. This is
25 especially true during the hot-topping phase, where the top radiation plays an increasingly
26 important role as compared to the arc energy input. Thus, whereas the crude model has the
27 advantage of its simplicity, use of the detailed model should be preferred.
28

29

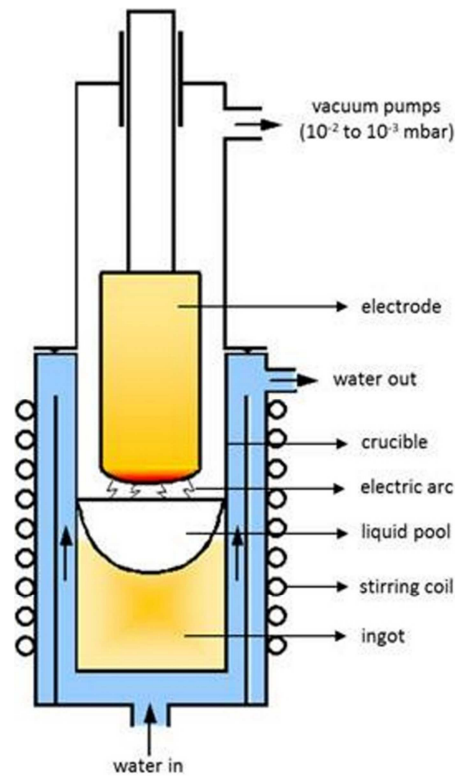
30

31

Introduction

32 Vacuum Arc Remelting (VAR) is a metallurgical process used for the production of high
33 quality ingots of special steel or nickel-based superalloy. It is also the final stage in the
34 melting cycle of reactive metals such as titanium and zirconium alloys. A detailed
35 understanding of the VAR process is of prime importance because of the strategic role and
36 high market value of those alloys ¹. The VAR process, as illustrated in Figure 1, involves
37 melting a consumable metallic electrode under a high vacuum to form a secondary ingot with
38 a good structural quality. Melting of the electrode is assured by an electric arc maintained
39 between the electrode tip (acting as the cathode) and the top of the ingot (acting as the anode).
40 The liquid metal drops formed at the electrode tip fall through the arc plasma and
41 progressively build up the ingot, which solidifies in contact with the walls of a water-cooled
42 copper crucible. This ingot is composed of three parts: the liquid pool, the fully solidified
43 metal and the intermediate mushy zone. The electric arc can be confined by an axial magnetic
44 field created by an external induction coil in order to stabilize the arc. This magnetic field is
45 also used to stir the liquid metal, in order to enhance the chemical homogeneity of the ingot.

46



47
48

Figure 1: VAR process schematic representation.

49

50 The energy flux at the ingot top plays a key role in the process, as it has a direct effect on the
 51 temperature and velocity fields in the molten metal, which both determine the local
 52 solidification conditions. The total energy flux at the ingot top may be divided into three main
 53 contributions: the heat stored in the incoming drops, the energy input from the arc plasma, and
 54 the net radiative energy flux at the ingot top surface. In the present paper, we will concentrate
 55 on this latter contribution. Note that the radiative energy flux is expected to be much smaller
 56 than the two other input energy fluxes during most of the melt, yet its contribution may
 57 become more important during the hot-topping stage at the end of the melt, which is
 58 performed with a reduced arc power.

59

60 One of the classical approaches adopted to study the VAR process is based on the
 61 development of a mathematical CFD model that describes the ingot growth and solidification

62 during a VAR operation. Several such models have been described in the literature. They
63 involve solving the conservation equations of mass, momentum and energy, while accounting
64 for turbulence and electromagnetic effects in the molten pool as well as the solidification of
65 the metal. The majority of the models consider a 2D axisymmetric geometry. One of those
66 model is SOLAR ². Another one is the model MeltFlow-VAR ³. However, with the aim of
67 better taking into account the precise distribution and possible motion of the arc, Pericleous et
68 al. ⁴ have recently proposed a model based on a 3D geometry. Moreover, their macromodel
69 was coupled to a microscale simulation of the solidification process.

70

71 As far as the description of the ingot top thermal radiation is concerned, the only detailed
72 work dealing with that subject we are aware of is due to Ballantyne ⁵ who represented the
73 radiative heat transfer in a VAR furnace using an electrical network analogy based on the
74 radiosity method. This method takes into account the radiative heat exchanges between all
75 surfaces elements inside the furnace. The radiation model was combined with simplified ingot
76 and electrode models, allowing the prediction of the melt rate and liquid pool depth values,
77 which were found to be in good agreement with measurements ⁵.

78

79 In the present paper, we describe our model for evaluating the ingot top radiation similar to
80 that derived by Ballantyne ⁵. Our proposed model is then incorporated into a CFD
81 macromodel developed at Nancy, that allows computation of the growth and solidification of
82 a VAR ingot. Then we compare the thermal and velocity fields inside the ingot predicted by
83 that model with results obtained using a crude one, based on a simplified description of the
84 radiative heat exchanges.

85

86

II Models

87 In the radiative heat transfer models presented below, two main hypotheses are made. The
88 first hypothesis is that the arc plasma in the interelectrode region is transparent to thermal
89 radiation. There are two main reasons why we decided to consider that the arc is transparent
90 to thermal radiation. The volume fraction of macroparticles in the plasma (mainly tiny liquid
91 metal droplets ejected at the cathode surface) is extremely low, so the absorption of radiation
92 within the arc is probably not important. In addition, it is widely accepted in the vacuum arc
93 literature that (at low current density levels similar to those employed in a VAR furnace) the
94 power radiated by the arc represents a negligible fraction of the total arc power ⁶ hence
95 radiation from the plasma may be neglected. More detailed data on the radiative properties of
96 the electric arc in VAR would be needed for a more refined model. It is interesting to mention
97 that Ballantyne ⁷ found that the arc cannot be considered as opaque. The second assumption is
98 that all surfaces are considered as grey and diffusive surfaces. Thus, their emissivity ϵ
99 depends only on the surface material and the material state (solid or liquid). Two approaches
100 for calculating the flux radiated from the ingot top surface are described below. The first
101 approach is a simplified model that does not account for the fill ratio, hence directly uses the
102 Stefan-Boltzmann law. The second approach is a more detailed model based on the radiosity
103 method.

104

105 ***II.1 Simplified model: Stefan-Boltzmann law***

106 In this model, the net energy flux density radiated by each surface element i of the ingot top
107 M_i^{net} (in W/m^2) is simply calculated from the Stefan-Boltzmann law ⁸:

$$M_i^{net} = \epsilon_i \sigma (T_i^4 - T_{elec}^4) \quad (1)$$

108 where $\sigma = 5.67 \times 10^{-8} W \cdot m^{-2} \cdot K^{-4}$ is the Stefan-Boltzmann constant, T_i is the temperature
109 of surface i and T_{elec} is the temperature of the liquid film covering the electrode tip. This
110 approach in fact considers that the electrode diameter is identical to that of the ingot (fill ratio

111 equal to 1) and neglects the contributions of the crucible and the annular gap between the
112 crucible and electrode in the radiative exchanges. Because the ingot top is assumed to radiate
113 in an environment at a higher temperature than in reality, the radiative heat fluxes and thus the
114 energy loss of the ingot will be underestimated.

115

116 ***II.2 Advanced model: Radiosity method***

117 In this model inspired by the work of Ballantyne ⁶, the flux radiated from the ingot top surface
118 is calculated considering all radiative exchanges inside the furnace, i.e. taking into account the
119 radiation between the ingot top surface, the tip and lateral surface of the electrode and the
120 crucible wall. This requires calculating the radiative heat fluxes from each of these surfaces.
121 The model described here uses the radiosity method ⁷.

122

123 The radiosity represents the radiation flux density leaving a given surface i and is defined (for
124 an opaque surface) as the sum of the emitted and reflected radiation flux densities:

$$J_i = \varepsilon_i \sigma T_i^4 + (1 - \varepsilon_i) \sum_{j=1}^n F_{i,j} J_j \quad (2)$$

125 In this equation, the reflected flux density has been written as a function of geometrical view
126 factors, $F_{i,j}$. The view factor $F_{i,j}$ between the surfaces i and j is the proportion of the total
127 radiative flux leaving surface i that reaches j . One should mention three useful relationships
128 between view factors. View factors obey a reciprocity relationship $S_i F_{i,j} = S_j F_{j,i}$, where S_i
129 and S_j are the areas of surfaces i and j . The sum of the view factors from a given surface is
130 unity (known as the summation rule): $\sum_j F_{i,j} = 1$. Yet another useful relation comes from the
131 superposition rule, by which the view factor to a surface is, at large scale, the sum of the view
132 factors to the parts of that surface: $F_{i,j+k} = F_{i,j} + F_{i,k}$. Note that view factors are tabulated in
133 the literature for many specific configurations. For complex configurations, view factors may

134 be determined using a Monte-Carlo ray tracing method. For a system of n surfaces forming an
135 enclosure, one obtains from (2) a system of n linear algebraic equations for the determination
136 of the n unknown radiosities. Once the radiosities have been determined, the net energy flux
137 density radiated by a surface element i of the ingot top may be calculated from the following
138 relation:

$$M_i^{net} = \frac{\varepsilon_i}{1 - \varepsilon_i} (\sigma T_i^4 - J_i) \quad (3)$$

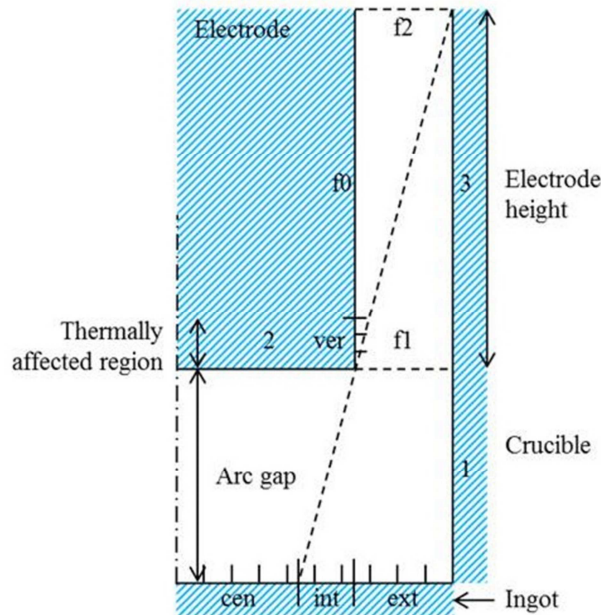
139 Note that in the above procedure, the surface temperature must be given for each surface.

140

141 Figure 2 presents the geometrical configuration considered in our model, detailing every
142 surface involved for the calculation of the ingot top thermal radiation. Surfaces 1 and 3
143 describe the crucible wall. As it will appear below, the crucible wall was divided into two
144 surfaces to make the calculation of some of the view factors easier. Surface 2 represents the
145 bottom surface of the electrode. Along the lateral surface of the electrode, two regions are
146 distinguished. The first region (*ver*) corresponds to the lower part of the electrode, where a
147 strong vertical variation of the temperature takes place. The second region (surface *f0*)
148 corresponds to the upper part of the electrode, where the temperature can be considered as
149 uniform. Note that region *ver* is subdivided into several surface elements, in order to better
150 take into account the temperature variation in this region. The ingot top surface is divided into
151 three regions. The first region (*cen*) corresponds to the portion of the top surface, which does
152 not see the surface *f2* (see Figure 2). The second region (*int*) corresponds to the portion of the
153 top surface, which is able to see the surface *f2* but not the lateral surface of the electrode.
154 Finally, the third region (*ext*) corresponds to the aiming portion of the top surface (in the
155 annulus zone), which is able to see all other surfaces of the domain. Similarly to region *ver*,
156 each of these three regions is subdivided into several surface elements of uniform temperature
157 in order to take into consideration the temperature variation over the ingot top surface.

158 Finally, surfaces $f1$ and $f2$ are both virtual surfaces that do not radiate any heat. Surface $f1$ is
 159 introduced to make easier the calculation of several view factors. Surface $f2$ is employed to
 160 close the domain.

161



162
 163

Figure 2: Top furnace schematic representation in the radiation model.

164

165 Almost all the view factors involved in our model may be computed using formula tabulated
 166 in the literature. The view factors tabulated formula used in this model can be found in the
 167 publication of Leuenberger and Person⁹ for the view factors between disks, rings and surfaces
 168 of a cylindrical geometry, Buschmann and Pittman¹⁰ for the view factors between surfaces of
 169 sections of cylinder and Brockmann¹¹ for the view factors between surfaces of two concentric
 170 cylinders. However, for a few complex view factors, no formulas are available and their
 171 evaluation relies on some approximations which are detailed below. This concerns in
 172 particular pairs of surfaces for which the sight of view is partially occulted by the electrode.

173

174 *Calculation of $F_{f2,1}$*

175 The evaluation of the view factor $F_{f2,1}$ is based on the superposition principle:

$$F_{f2,1} = F_{f2,1+3} - F_{f2,3} \quad (4)$$

176 The view factor between surface $f2$ and the combination of surfaces 1 and 3 is calculated from
 177 a tabulated formula by considering that the electrode is an infinite cylinder. Note that such an
 178 approach is valid as long as the surface $f2$ does not see the surface 1 through the interelectrode
 179 gap, i.e. as long as the height of the electrode is much larger than the interelectrode gap. The
 180 view factor $F_{f2,3}$ in (4) is calculated using a tabulated formula without any assumption
 181 regarding the height of the electrode.

182

183 *Calculation of $F_{int_i,f2}$ and $F_{ext_i,f2}$*

184 The view factor between any surface h ($h=\{int_i, ext_i\}$) at the ingot top and the surface $f2$ is
 185 calculated using the following approximation:

$$F_{h,f2} = F_{h,3+f2} \times F_{f1,f2}/F_{f1,3+f2} \quad h = \{int_i, ext_i\} \quad (5)$$

186 This amounts considering that the ratio of the solid angle between surfaces h and $f2$ over the
 187 solid angle between h and $(3+f2)$ is identical to the ratio of the solid angle between $f1$ and $f2$
 188 over the solid angle between $f1$ and $(3+f2)$. This equation is an approximation for calculating
 189 view factor $F_{h,f2}$. In (5), the view factors $F_{f1,f2}$ and $F_{f1,3+f2}$ are obtained from tabulated
 190 formula, whereas the view factor $F_{h,3+f2}$ is calculated by:

$$F_{h,3+f2} = 1 - \sum_{k \in \{3;f2;f1\}} F_{h,k} \quad h = \{int_i, ext_i\} \quad (6)$$

191

192 *Calculation of $F_{1,3}$, $F_{int_i,3}$ and $F_{ext_i,3}$*

193 The determination of the view factors $F_{h,3}$ ($h = \{1, int_i, ext_i\}$) is based on the summation
 194 rule:

$$F_{h,3} = 1 - \sum_{k \notin \{3;f1\}} F_{h,k} \quad h = \{1, int_i, ext_i\} \quad (7)$$

195 Because of the approximations made when evaluating $F_{h,f2}$ ($h = \{1, int_i, ext_i\}$), the values of
 196 $F_{h,3}$ ($h = \{1, int_i, ext_i\}$) obtained by this relation should be considered as approximated
 197 values.

198

199

III Verification

200 In this section, our intention is to determine and discuss the influence of the assumptions
 201 made in the model described above when evaluating the non-tabulated view factors. For this
 202 purpose, exact values of these view factors have been determined using the Monte-Carlo ray
 203 tracing method ¹².

204

205 This method consists of several steps. The first step is to select randomly the coordinates (R ,
 206 α) of the starting position of a ray on the emitting surface. In the second step, the emission
 207 direction of the ray is defined by selecting randomly a couple of angles (θ , φ). The third step
 208 is to track the trajectory of the emitted ray and determine the first surface it will intercept. All
 209 steps are repeated for a very large number of rays, so that the sample size is statistically
 210 significant. Finally, the view factor between the emitting surface and a given surface
 211 corresponds to the ratio of the number of times that surface was hit to the total number of rays
 212 emitted. The parameters R , α , θ and φ are defined as follows:

$$R = r_i + (r_e - r_i) * \sqrt{n_1} \quad (8)$$

$$\alpha = 2\pi * n_2 \quad (9)$$

$$\theta = 2\pi * n_3 \quad (10)$$

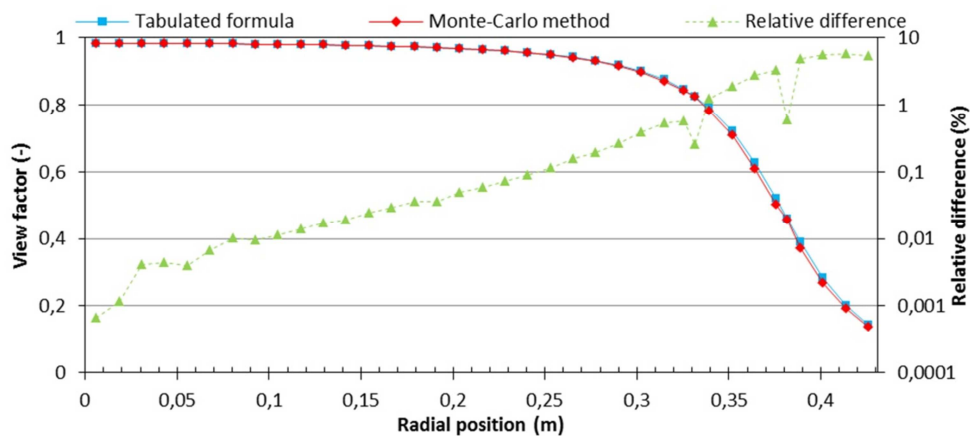
$$\varphi = \sin^{-1}(\sqrt{n_4}) \quad (11)$$

213 where n_i are independent random numbers between 0 and 1 and r_i (resp. r_e) is the inner (resp.
214 outer) radius of the annular shape emitting surface ($r_i = r_e$ (resp. $r_i = 0$) in the case of
215 cylindrical (resp. disk) shape surfaces).

216

217 Before using the Monte-Carlo ray tracing method to determine the approximated view factors,
218 the correct implementation of the method was checked by applying the method to calculate
219 known tabulated view factors, namely the view factors between surface elements at the ingot
220 top and the electrode bottom surface (surface 2). Figure 3 compares the values of the view
221 factor obtained with the tabulated formula with those computed with the Monte-Carlo method
222 (considering 10^8 rays for each surface).

223



224

225 **Figure 3: View factor between a surface element at the ingot top and the bottom surface**
226 **of the electrode. Comparison between results obtained with tabulated formulas and**
227 **results determined with the Monte-Carlo method. Calculations performed for an ingot**
228 **radius of 0.432 m, an electrode radius of 0.381 m and an arc gap of 0.05 m.**
229

230 Figure 3 shows that both methods give very similar values of the view factors, with a relative
231 difference between the two results less than a few percent, which may be attributed to the
232 statistical nature of the Monte-Carlo results. Quite logically, the increase in the relative
233 difference with the radial position is related to the decrease of the view factor. So, the good

234 agreement between both calculation methods validates our implementation of the Monte-
235 Carlo ray tracing method.

236

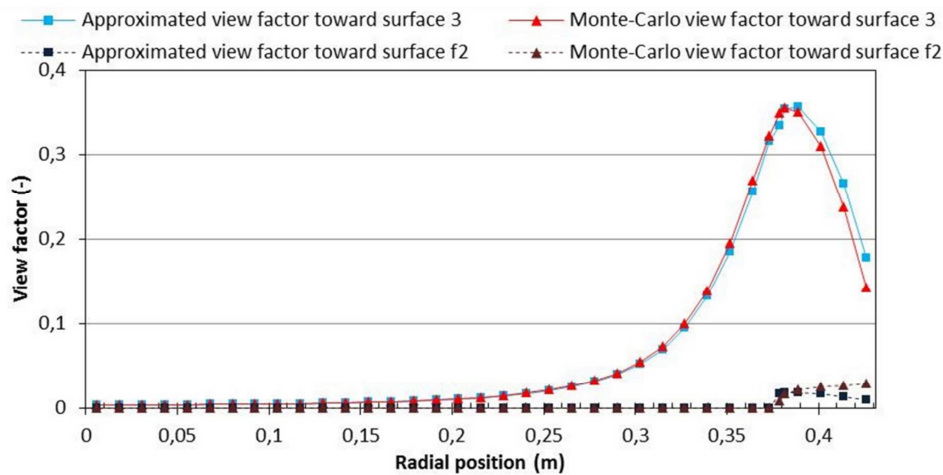
237 Having checked that the Monte-Carlo method is correctly implemented, we then apply the
238 method to determine the view factors, whose evaluation in section II is based on
239 approximations (Eqs. (4) to (7)).

240

241 Considering first the view factors $F_{1,3}$ and $F_{f2,1}$, we recall that an approximation is used to
242 estimate those view factors only when the electrode height is smaller than the arc gap. Table 1
243 compares for such conditions the values of those view factors obtained using the proposed
244 approximations with their values obtained using the Monte-Carlo method. The approximated
245 view factors exhibit a significant error. Yet, as it will be shown later, due to the small absolute
246 values of those view factors, the error induced by the approximations has a very low impact
247 on the evaluation of the flux radiated at the ingot top, which is the parameter of main interest
248 in the present study.

249

250 In Figure 4, the values of the view factors between surface elements at the ingot top and
251 respectively surfaces $f2$ and 3 calculated using the approximations described in section II are
252 compared to the values obtained with the Monte-Carlo method. First it should be pointed out
253 that the results given by our model for surface elements located in the central region (*cen*)
254 (which extends up to 0.3759 m) are naturally in very good agreement with the Monte-Carlo
255 results, since our model employs a tabulated formula in this region. In the intermediate and
256 external regions, we observe in contrast that the approximated view factors are slightly
257 different from the Monte-Carlo view factors. Moreover, Figure 4 shows a trend to larger
258 discrepancies when one approaches the crucible wall.



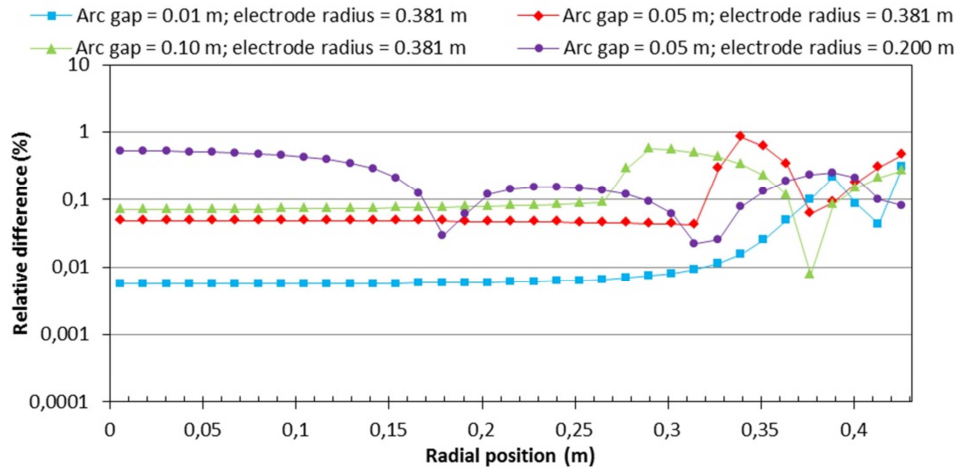
260

261 **Figure 4: View factor from surface elements of the ingot top toward surface 3 and**
 262 **surface f_2 obtained using the approximate method and the Monte-Carlo method.**
 263 **Calculations performed for an ingot radius of 0.432 m, an electrode radius of 0.381 m,**
 264 **an electrode height of 0.5 m and an arc gap of 0.05 m.**

265

266 Finally, the ability of our model to compute with a good accuracy the heat flux density
 267 radiated from every location at the ingot top, despite the approximations made when
 268 evaluating the non-tabulated view factors, is tested. Our model predictions are compared with
 269 a result determined with the non-tabulated view factors being obtained from the Monte-Carlo
 270 method. Figure 5 presents the relative difference between the two results for various
 271 conditions relative to the end (short electrode) of a VAR melt. The emissivity values and the
 272 temperature of every surface of the domain considered in those calculations are given
 273 respectively in Table 2 and in Table 3. The thermophysical properties of Ti-6-4 alloy required
 274 for the simulation were taken from Valencia and Queded¹³ except for the emissivity which is
 275 taken from Boivineau et al.¹⁴.

276



277

278 **Figure 5: Relative difference in the heat flux density radiated at the ingot top depending**
 279 **on the calculation method (approximate and Monte-Carlo methods) of the non-**
 280 **tabulated view factors for an electrode height of 0.05 m.**

281

282 Figure 5 shows that the approximations made when evaluating the non-tabulated view factors
 283 have a negligible impact on the radiative heat flux density computed at the ingot top for all
 284 tested configurations. This result may be explained by the fact that the approximations
 285 concern view factors toward a surface which either has a low temperature (surface 3) as
 286 compared to that of the ingot top or does not emit any radiation (surface f_2). Therefore, the
 287 radiative fluxes originating from these surfaces have a negligible influence on the
 288 computation of the radiation emitted at the ingot top. The only case where the approximations
 289 could have an impact would be when the temperature of the ingot top is of the same order of
 290 magnitude as that of surface 3. This could occur during the cooling phase of the ingot after
 291 extinction of the arc. Finally, it must be noted that the Monte-Carlo ray tracing method has a
 292 high computational cost. Because of this cost and given the negligible impact on the ingot top
 293 radiation of a precise calculation of the non-tabulated view factors using the Monte-Carlo
 294 method, we decided hereafter to evaluate those non-tabulated view factors not by the Monte-
 295 Carlo method but using the approximations described in Section II.

296

297

IV Radiation model results

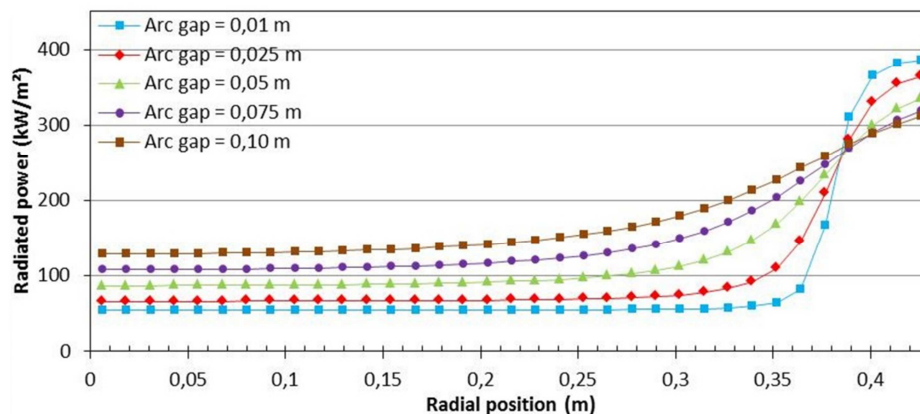
298 This section is separated into two parts. The first part is a parametric study, aimed at
 299 analysing the influence of various geometric parameters on the heat flux density radiated at
 300 the ingot top. In the second part, we describe the integration of the two proposed radiation
 301 models (i.e. the simplified and advanced models) in the CFD software SOLAR² which
 302 simulates the growth and solidification of a VAR ingot. Then we compare the ingot
 303 simulation results obtained with the two models.

304

305 *IV.1 Impact of the geometric parameters on the ingot top radiation*

306 In this section, we apply the detailed radiation model to calculate the radial profile of the heat
 307 flux density radiated at the ingot top and we investigate the influence of various geometric
 308 parameters on this profile. The model is applied to an electrode and an ingot made of Ti-6-4
 309 alloy, whose emissivity is given in Table 2, and the surface temperatures are given in Table 3.
 310 The temperature at the ingot top surface is considered to be uniform. All calculations have
 311 been performed with a mesh of 35 surfaces at the ingot top and 10 surfaces in the region *ver*
 312 along the lateral surface of the electrode. The influences of a variation of the arc gap,
 313 electrode radius and electrode height on the profile of the heat flux density radiated at the
 314 ingot top are illustrated in Figures 6 to 8.

315

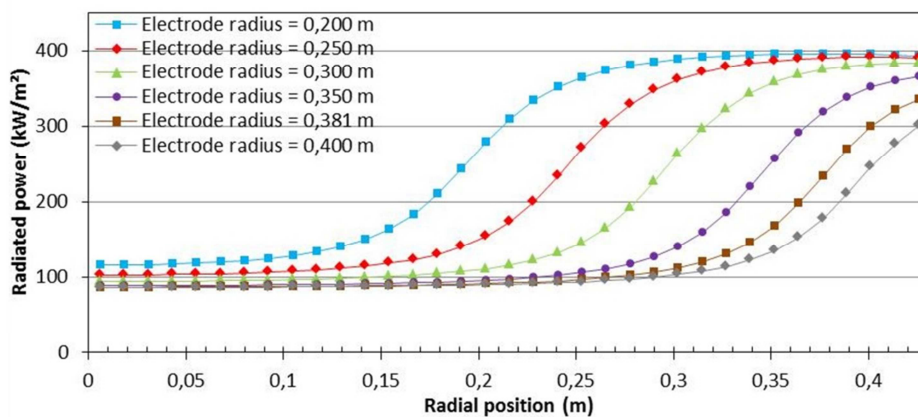


316

317 **Figure 6: Ingot top radiation for different arc gaps.** Calculations performed for an ingot
 318 radius of 0.432 m, an electrode radius of 0.381 m and an electrode height of 1.5 m.
 319

320 It is observed that the ingot top radiation depends heavily on the arc gap and the electrode
 321 radius. The smaller the arc gap, the larger the difference between the radiative flux density
 322 emitted by ingot surface elements located underneath the electrode and that emitted by ingot
 323 surface elements located below the annular gap between the electrode and crucible. This can
 324 be explained as follows. In the case of short arc gaps, the ingot surface elements located
 325 underneath the electrode see mainly the tip of the electrode (surface 2) which has a
 326 temperature similar to that of the ingot, yielding small radiative heat flux densities. By
 327 contrast, the ingot surface elements located below the annular gap see mainly surfaces which
 328 have a low temperature, which implies larger radiative heat flux densities. When the arc gap
 329 increases, the fraction of the solid angle of the ingot surface elements located underneath the
 330 electrode which is occupied by the "cold" surfaces increases, leading to an increase in the
 331 radiation. On the other hand, the fraction of the solid angle of the ingot surface elements
 332 located below the annular gap which is occupied by the tip of the electrode will also increase,
 333 leading to a decrease of the radiation.

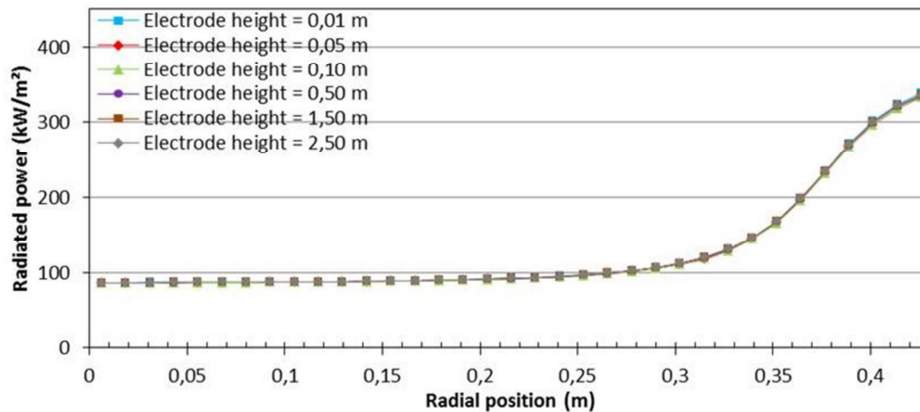
334



335

336 **Figure 7: Ingot top radiation for different electrode radii.** Calculations performed for an
 337 ingot radius of 0.432 m, an electrode height of 1.5 m and an arc gap of 0.05 m.
 338

339 As it was expected, a variation of the electrode radius strongly affects the location of the
 340 transition between the low radiation region below the electrode and the high radiation region
 341 below the annular gap. Again, this may be explained considering the proportion of the solid
 342 angle of the ingot surface elements located underneath the electrode which is occupied by the
 343 "hot" surface of the electrode (surface 2). The greater the electrode radius, the larger the
 344 number of surface elements seeing mainly surface 2, which results in an increase of the low
 345 radiation region at the ingot top. This explains the apparition of an isosbestic point on figure 6
 346 at approximately 0.38 m, which is closed to the constant electrode radius.
 347



348
 349 **Figure 8: Ingot top radiation for different electrode heights. Calculations performed for**
 350 **an ingot radius of 0.432 m, an electrode radius of 0.381 m and an arc gap of 0.05 m.**
 351

352 In contrast to the variations in the arc gap and electrode radius, a change of the electrode
 353 height has a negligible influence on the ingot top radiation. The height of the electrode
 354 impacts essentially the proportion of the flux radiated by the ingot toward surfaces 3, f0 and
 355 f2, and the surfaces composing the region ver. Except for the latter, those surfaces have
 356 similar low temperature. Therefore, the heat flux density radiated at the ingot top is only little
 357 affected by a variation in the electrode height.

358

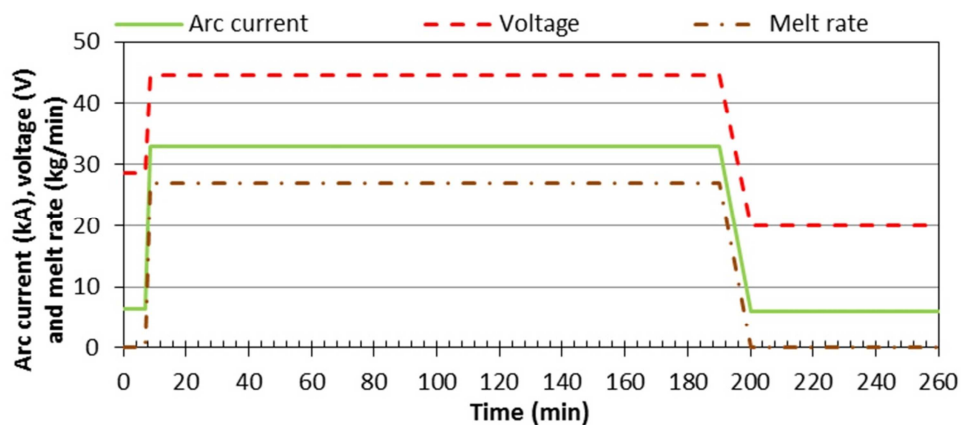
359 *IV.2 Impact of the radiation model on the Ti-6-4 melt simulation results*

360 The two radiation models described in section II have been integrated into the CFD
361 macromodel SOLAR¹⁵. In this section, we simulate the melt of a Ti-6-4 electrode and
362 compare the results obtained using both radiation models.

363

364 The operating parameters of the simulated melt are as follows. The melt consists of two main
365 sequences. The first main sequence (seq. 1) lasts 181.2 min. During this sequence, the arc
366 current is set to 33 kA, the voltage is set to 44.7 V and the melt rate is set to 27 kg/min. Note
367 that these values are taken from the work of Patel et al.¹⁶. Before this sequence, the arc
368 current, arc voltage and melt rate were set to 6.5 kA, 28.5 V and 0 kg/min during 6.8 min then
369 increased progressively during 2 min from these values to the ones of the first main melt
370 sequence. The second sequence (seq. 2), which corresponds to the hot-topping stage, lasts 60
371 min. During this sequence, the arc current is set to 6 kA, the arc voltage to 20 V and the melt
372 rate to zero. Between sequence 1 and sequence 2, the arc current, voltage and melt rate are
373 progressively decreased during 10 min. Figure 9 presents the time evolution of those
374 parameters. During all the melt, a constant unidirectional stirring with a magnetic field of 1.4
375 mT is applied.

376



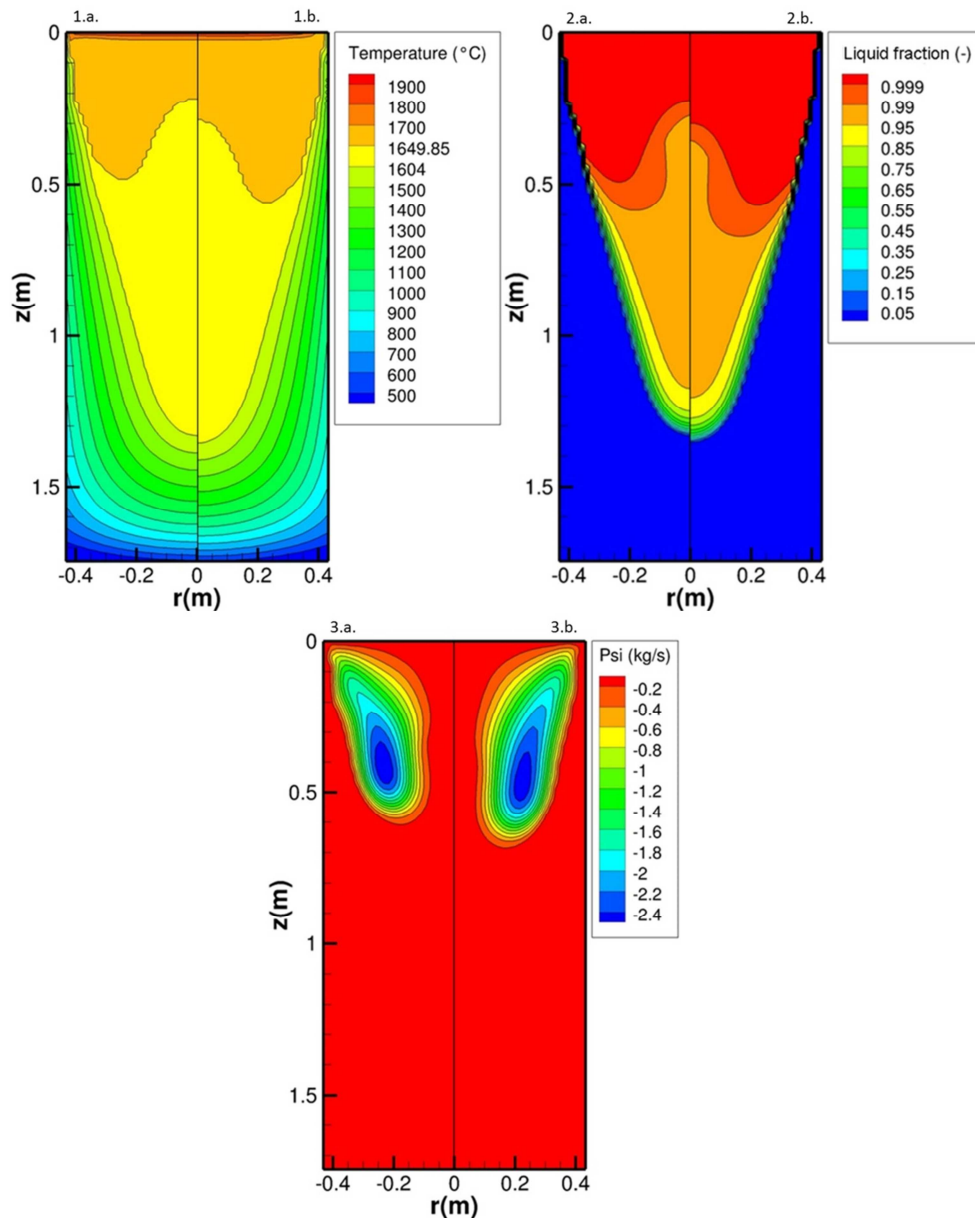
377

378

Figure 9: Operating parameters of the simulated melt.

379

380 We first analyze the effect of the radiation modelling method on the simulation results during
 381 the first sequence of the melt. Figures 10 to 12 present at a given moment during this
 382 sequence, respectively the ingot temperature field, liquid fraction map and stream function of
 383 the liquid metal motion in the molten pool.
 384



385

386 **Figure 10: (1) Ingot temperature field, (2) liquid fraction map and (3) stream function**
 387 **map in the molten pool at a given time during the first sequence of the melt, computed**
 388 **with the (a) simplified and (b) advanced radiation models.**

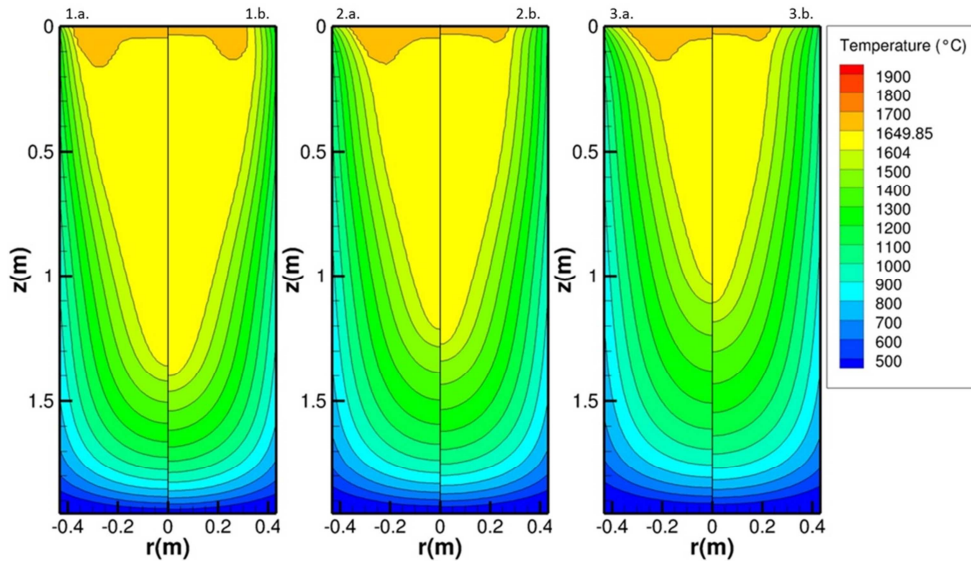
389

390 In this figure, we observe only small differences between the two models. Use of the
391 advanced radiation model predicts similar temperature at the ingot top (with a deviation of a
392 few percent) but induce a notable different temperature field in the ingot, with a deeper pool.
393 This result is related to the lower power radiated energy at the ingot top in the case of the
394 advanced model (86.8 kW versus 88.6 kW with the simplified model) and the modification of
395 the distribution of this radiation flux. The advanced model induces higher radiation at the
396 ingot edge, as compared to the simplified model which causes locally a slightly inferior
397 temperature. This decrease in the temperature results in a net diminution (by about 5%) of the
398 energy lost at the mold wall.

399

400 The differences between the results obtained using the two radiation models tend to be more
401 important during the hot-topping stage. This is due to the much smaller energy provided by
402 the arc during this sequence, resulting in a more important contribution of the thermal
403 radiation in the energy balance at the ingot top. These differences are illustrated in Figure 11,
404 which shows the evolution of the ingot temperature field during the hot-topping, predicted by
405 both radiation models. Figure 12 presents the local solidification time in the ingot at the end
406 of the melt. The area with a local solidification time equal to 0 corresponds to the non-fully
407 solidified ingot (i.e. liquid pool and mushy zone). Again, the model with a more detailed
408 description of radiative heat exchanges leads to a deeper mushy zone and a modification in
409 the liquid pool shape. In particular the detailed model leads to lower temperature values at the
410 ingot top surface near the crucible wall. The increase in the radiation predicted with the
411 advanced model is the cause of an earlier solidification near the ingot edge. Furthermore, it
412 leads to a slightly lower of the local solidification time mostly at the ingot top.

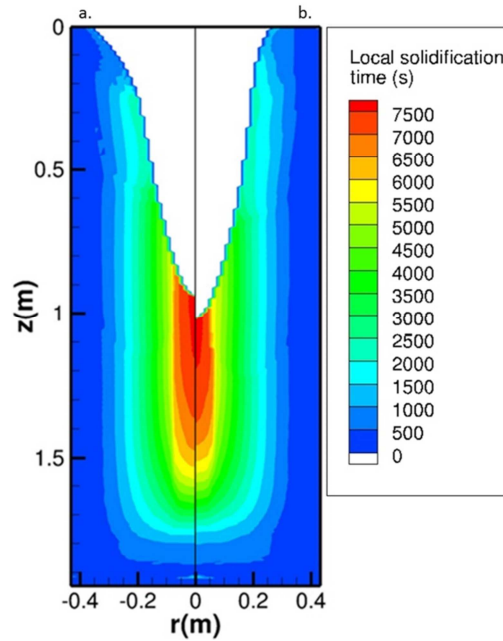
413



414

415 **Figure 11: Ingot temperature field during the hot-topping stage computed with the (a)**
 416 **simplified and (b) advanced radiation models at three given moments: (1) 10 min, (2) 30**
 417 **min and (3) 50 min after the beginning of the hot-topping stage.**

418



419

420 **Figure 12: Computed local solidification time in the fully solidified ingot with the (a)**
 421 **simplified and (b) advanced radiation models at the end of the melt.**

422

423

Conclusion

424

A numerical investigation of the ingot top thermal radiation in the vacuum arc remelting

425

process was undertaken. Two different approaches have been compared for the calculation of

426 the radiation emitted at the ingot top, namely a crude approach that considers only the
427 radiative heat transfer between the ingot and the electrode tip, with a simplified representation
428 of the electrode geometry, and a more detailed approach based on the radiosity method and
429 taking into account all radiative exchanges between the ingot, electrode and crucible wall. In
430 both cases, all surfaces are assumed as diffusive grey ones and the arc is neglected. This
431 second approach relies on some approximations for the evaluation of non-tabulated view
432 factors. Yet, it was verified from Monte-Carlo ray tracing simulations that those
433 approximations have a negligible influence on the computed ingot top radiation. Results of
434 the detailed radiation model revealed that the ingot top radiation is heavily dependent on the
435 arc gap length and the electrode radius. By contrast, it is almost independent on the electrode
436 height. Finally, the two proposed radiation models were implemented within a numerical code
437 that simulates the growth and solidification of a VAR ingot. In the case of a Ti-6-4 melt, we
438 have shown that the use of the detailed radiation model has a slight effect on the ingot
439 simulation results when compared to these obtained with the crude radiation modelling
440 approach, especially during the hot-topping stage. The replacement of the radiation model
441 leads to a modification, among others, the ingot energy balance, of the ingot temperature
442 field, the liquid pool shape and depth and the local solidification time. A precise modeling of
443 the ingot solidification in industrial cases justifies the interest of using a detailed radiation
444 modelling approach that considers all radiative surfaces present above the ingot top, as
445 proposed in the present work.

446

447

References

- 448 1. L.A. Bertram, R.S. Minisandram and K.O. Yu: *Modeling for casting and solidification*
449 *processing*, 1st, Marcel Dekker Inc., New York, NY, 2002. pp. 565–612.
- 450 2. A. Jardy and D. Ablitzer: *Rare Met. Mater. Eng.*, 2006, 35, vol. 1, pp.119-122.

- 451 3. K.M. Kelkar, S.V. Patankar, A. Mitchell, O. Kanou, N. Fukada and K. Suzuki: *World Conf.*
452 *Titanium, 11th*, Kyoto, Japan, June, 3-7, The Japan Institute of Metal, Sendai, 2007, pp. 1279-
453 1282.
- 454 4. K. Pericleous, G. Djambazov, M. Ward, L. Yuan and P.D. Lee: *Metall. Mater. Trans. A*,
455 2013, vol. 44, no.12, pp. 5365–5376.
- 456 5. A.S. Ballantyne: *Proc. 2013 Int. Symp. on Liquid Metal Processing and Casting*, Austin,
457 TX, Sept. 22-25 2013, M.J.M. Krane, A. Jardy, R.L. Williamson, J.J. Beaman, 2013, pp. 253-
458 259.
- 459 6. A. Anders and S. Anders: *J. Phys. D: Appl. Phys*, 1991, vol. 24, pp. 1986–1992.
- 460 7. A.S. Ballantyne: *Proc. 2015 Int. Symp. on Liquid Metal Processing and Casting*, Leoben,
461 Austria, Sept. 20-24, 2015, A. Kharicha, R.M. Ward, H. Holzgruber, M. Wu, 2015, pp. 244-
462 254.
- 463 8. J. Sucec: *Heat transfer*, 1st ed., Simon & Schuster, New York, NY, 1975, 604 pp.
- 464 9. H. Leuenberger and R.A. Person: *Am. Soc. Mech. Eng.*, 1956, 56-A-144.
- 465 10. A.J. Buschman and C.M. Pittman: *NASA*, 1961, NASA-TN D-944.
- 466 11. H. Brockmann: *Int. J. Heat Mass Transf.*, 1994, vol. 37, no. 7, pp. 1095-1100.
- 467 12. H.W. Jensen, J. Arvo, P. Dutre, A. Keller, A. Owen, M. Pharr and P. Shirley: Monte Carlo
468 Ray Tracing, 2003, <http://www.cs.odu.edu/~yaohang/cs714814/Assg/raytracing.pdf>.
- 469 13. J.J. Valencia and P.N. Quested: *ASM Handbook*, 2008, vol. 15, pp. 468-481.
- 470 14.M. Boivineau, C. Cagran, D. Doytier, V. Eyraud, M.-H. Nadal, B. Wilthan and G.
471 Pottlacher: *Int. J. of Thermophys.*, 2006, vol. 27, no.2, pp. 507-529.
- 472 15. A. Jardy and D. Ablitzer: *Mater. Sci. Technol.*, 2009, vol. 25, pp. 163-69.
- 473 16. A. Patel, D.W. Tripp and D. Fiore: *Proc. 2013 Int. Symp. on Liquid Metal Processing and*
474 *Casting*, Austin, TX, Sept. 22-25 2013, M.J.M. Krane, A. Jardy, R.L. Williamson, J.J.
475 Beaman, 2013, pp. 241-244.

476

477

Tables

| | Approximate method | Monte-Carlo method |
|------------|-----------------------|-----------------------|
| $F_{1,3}$ | 0.01718328 | 0.03141745 |
| $F_{f2,1}$ | 0.16533963 | 0.13567865 |

478 **Table 1: Comparison of the values of the view factors $F_{1,3}$ and $F_{f2,1}$ obtained using the**
 479 **approximate method and the Monte-Carlo method. Calculations performed for an ingot**
 480 **radius of 0.432 m, an electrode radius of 0.381 m, an electrode height of 0.05 m and an**
 481 **arc gap of 0.1 m.**
 482

| | Emissivity |
|--------------|------------|
| Crucible | 0.8 |
| Liquid metal | 0.428 |
| Solid metal | 0.58 |

483

Table 2: Emissivity values used in the simulations.

484

| Surface | Temperature | Comments |
|------------------------|--|---|
| 1 | 293.15 K | Ambient temperature |
| 2 | 1923 K | Liquidus temperature |
| 3 | 293.15 K | Ambient temperature |
| cen_i | 2023 K | Liquidus temperature + superheat of 100 K |
| int_i | 2023 K | Liquidus temperature + superheat of 100 K |
| ext_i | 2023 K | Liquidus temperature + superheat of 100 K |
| ver_i | Linear decrease of the temperature from the liquidus temperature (bottom) to the ambient temperature (top) | |
| f0 | 293.15 K | Ambient temperature |
| f1 | ∅ | |
| f2 | ∅ | |

485

Table 3: Temperatures of all surfaces used in the simulations.

486

487

Figure captions

488 Figure 1: VAR process schematic representation.

489 Figure 2: Top furnace schematic representation in the radiation model.

490 Figure 3: View factor between a surface element at the ingot top and the bottom surface of the
 491 electrode. Comparison between results obtained with tabulated formulas and results

492 determined with the Monte-Carlo method. Calculations performed for an ingot radius of 0.432
493 m, an electrode radius of 0.381 m and an arc gap of 0.05 m.

494 Figure 4: View factor from surface elements of the ingot top toward surface 3 and surface f2
495 obtained using the approximate method and the Monte-Carlo method. Calculations performed
496 for an ingot radius of 0.432 m, an electrode radius of 0.381 m, an electrode height of 0.5 m
497 and an arc gap of 0.05 m.

498 Figure 5: Relative difference in the heat flux density radiated at the ingot top depending on
499 the calculation method (approximate and Monte-Carlo methods) of the non-tabulated view
500 factors for an electrode height of 0.05 m.

501 Figure 6: Ingot top radiation for different arc gaps. Calculations performed for an ingot radius
502 of 0.432 m, an electrode radius of 0.381 m and an electrode height of 1.5 m.

503 Figure 7: Ingot top radiation for different electrode radii. Calculations performed for an ingot
504 radius of 0.432 m, an electrode height of 1.5 m and an arc gap of 0.05 m.

505 Figure 8: Ingot top radiation for different electrode heights. Calculations performed for an
506 ingot radius of 0.432 m, an electrode radius of 0.381 m and an arc gap of 0.05 m.

507 Figure 9: Operating parameters of the simulated melt.

508 Figure 10: (1) Ingot temperature field, (2) liquid fraction map and (3) stream function map in
509 the molten pool at a given time during the first sequence of the melt, computed with the (a)
510 simplified and (b) advanced radiation models.

511 Figure 11: Ingot temperature field during the hot-topping stage computed with the (a)
512 simplified and (b) advanced radiation models at three given moments: (1) 10 min, (2) 30 min
513 and (3) 50 min after the beginning of the hot-topping stage.

514 Figure 12: Computed local solidification time in the fully solidified ingot with the (a)
515 simplified and (b) advanced radiation models at the end of the melt.

516